NIH Public Access
Author Manuscript
Mol Imaging Biol. Author manuscript; available in PMC 2015 June 01.

Published in final edited form as:
Mol Imaging Biol. 2014 June ; 16(3): 330–339. doi:10.1007/s11307-013-0709-9.

Assessment of global cardiac uptake of Radiolabeled Iron Oxide Nanoparticles in Apolipoprotein E-Deficient Mice: implications for imaging cardiovascular inflammation

André Luís Branco de Barros[1,2,3,*], **Ann-Marie Chacko**[1], **John L. Mikitsh**[1], **Ajlan Al Zaki**[2], **Ali Salavati**[1], **Babak Saboury**[1], **Andrew Tsourkas**[2], and **Abass Alavi**[1,**]

[1]Divison of Nuclear Medicine and Clinical Molecular Imaging, Department of Radiology, Hospital of the University of Pennsylvania, Perelman School of Medicine, Philadelphia, PA, USA 19104

[2]Department of Bioengineering, University of Pennsylvania, Philadelphia, PA, USA, 19104

[3]Pharmacy School, Universidade Federal de Minas Gerais, Belo Horizonte, Minas Gerais, 31270-910, Brazil

Abstract

Purpose—Atherosclerosis is a leading cause of death in industrialized countries and is characterized by the accumulation of lipids and inflammatory cells, including macrophages, in blood vessel walls. Therefore, the ability to image macrophages could help identify plaques that are precursors of acute thrombotic events. Previous research has shown that long-circulating, nanoparticles could be used to detect macrophages within atherosclerotic plaques of the aorta. By conducting this study, we investigated whether global cardiac uptake of radiolabeled nanoparticles could allow assessment of total macrophage burden in the coronary arteries.

Procedures—Dextran-coated Iron Oxide Nanoparticles (IONPs) were labeled with iodine-125 via Bolton-Hunter (SHPP) method. IONPs were characterized by means of dynamic light scattering and transmission electronic microscopy. Biodistribution studies were performed in healthy and atherosclerotic mice. Additionally, digital autoradiography of hearts from both healthy and atherosclerotic mice was performed to assess regional and global atherosclerotic burden.

Results—The [^{125}I]IONPs exhibited high radiolabel stability and long blood circulation, which eventually led to high heart uptake in apoE −/− mice when compared with healthy controls. Furthermore, digital autoradiography showed substantially enhanced emission of signals from the hearts of atherosclerotic mice, while no or minimal cardiac signals were detected in healthy mice.

Conclusions—This preparation showed adequate physical-chemical properties for *in vivo* studies, such as small size (~30 nm), good radiolabel stability, and long circulation time. There was also significant accumulation in the heart of apoE−/− mice compared with that of healthy

**Corresponding author: Abass Alavi, MD, Division of Nuclear Medicine and Clinical Molecular Imaging, Department of Radiology, Hospital of the University of Pennsylvania, Perleman School of Medicine, Philadelphia, PA, USA 19104, abass.alavi@uphs.epenn.edu, Phone number: +1 215 662 3069; Fax number: +1 215-573-4107.
*First author: Pharmacy School, Universidade Federal de Minas Gerais, Belo Horizonte, Minas Gerais, 31270-910, Brazil, brancodebarros@yahoo.com.br, *Phone number:* +55 31 3409 6904; *Fax number:* +55 31 3409 6885

Conflict of interest
The authors declare that they have no conflict of interest.

NIH-PA Author Manuscript
NIH-PA Author Manuscript
NIH-PA Author Manuscript

NIH-PA Author Manuscript

NIH-PA Author Manuscript

NIH-PA Author Manuscript

control animals. These findings suggest that radiolabeled dextran-coated iron oxide nanoparticles may have potential to become a useful tool to detect macrophages in the atherosclerosis plaques of coronary arteries; however, these preliminary findings should be confirmed by further studies in a larger scale in various atherosclerosis models.

Keywords

Atherosclerosis; Radiolabeled nanoparticles; Diagnosis; Iron oxide nanoparticles; Global heart uptake

1 Introduction

Atherosclerosis is the leading cause of death in industrialized countries and is characterized by the accumulation of inflammatory cells and lipids in blood vessel walls. Formation of atherosclerotic plaques is a complex process initiated by an inflammatory response at the lesion site [1]. The disruption of plaques, and subsequent thrombus formation, is largely thought to stem from the accumulation of macrophages within the lesion [2]. Monocyte-derived macrophages play a critical role in atherogenesis from foam cells and fatty streak formation to the generation of proteinases that result in plaque disruption. High macrophage content in plaques characterizes vulnerability to rupture, which is intimately associated with clinical manifestation of atherosclerosis [3–6]. Macrophages can constitute more than 20% of the cells within an atheroma; therefore, the ability to image those macrophages could help identify plaques that are precursors of acute thrombotic events [7–8].

Nanoparticles that remain in circulation for an extended period of time are attractive candidates for the identification of macrophage burden in atherosclerotic plaques due to their ability to extravasate into inflamed tissue, where they are phagocytosed by macrophages. Several studies have already reported the use of nanoparticles (NP) to identify atherosclerosis in animal model of the disease, such as the apolipoprotein-E deficient mouse strain (apoE−/−) (*1*). In one study a sufficient amount of iron oxide nanoparticles (IONPs) were phagocytosed by macrophages within atherosclerotic plaques to be detectable by Magnetic Resonance Imaging (MRI)[9]. It has further been shown that there is an increase in the uptake of cross-linked dextran-coated iron oxide nanoparticles (CLIO) in plaques with high macrophage content, confirming the importance of macrophages in disease development and NP retention[10]. Although MRI has proven useful in detecting these abnormalities, optimal visualization often requires intravenous administration of large doses of IONP mass intravenously (2 to 20 mg Fe/kg) which may be associated with significant toxicity[11]. Radionuclide-based imaging techniques, such as positron-emission tomography (PET), offer sensitivity that is an order of magnitude higher than that of MRI (at least 1000 times), allowing administrating substantially lower concentrations of NP without affecting the quality of images generated [10–11]. Due to its high sensitivity, molecular imaging techniques with radiolabeled NPs may allow a paradigm shift for assessing macrophage burden in atherosclerotic plaques. We hypothesized that non-invasive global measurement of cardiac uptake of radiolabeled nanoparticles may could provide a means for assessment of macrophage burden in the coronary arteries and offer an opportunity for diagnosing early stages of atherosclerotic cardiovascular disease.

NIH-PA Author Manuscript

NIH-PA Author Manuscript

NIH-PA Author Manuscript

In this scientific communication, we describe the preparation and *in vivo* characterization of dextran-coated IONPs that can be labeled with radioactive iodine, such as iodine-125 and iodine-123 (for single photon emission computed tomography), and iodine-124 (for positron emission tomography). IONPs were surface modified with the water-soluble Bolton-Hunter reagent sulfosuccinimidyl-3-[4-hydroxyphenyl]propionate (SHPP) to enable direct electrophilic aromatic substitution of radioiodine, and physicochemical characterization was performed by means of dynamic light scattering (DLS) and transmission electronic microscopy (TEM). *In vitro* radiolabel stability, blood clearance, and biodistribution profiles of [125I]IONPs in control and apoE−/− mice were evaluated. Additionally, biodistribution studies and digital autoradiography (DAR) of hearts from both healthy and atherosclerotic mice was performed to further demonstrate diffuse uptake of this preparation in the hearts of affected mice.

2 Materials and Methods

2.1. Materials

Reagents were purchased from Sigma-Aldrich (St. Louis, MO, USA) and used as received, unless otherwise specified. [^{125}I]NaI (0.1 N NaOH, 2200 Ci/mmol) was purchased from Perkin Elmer (Boston, MA, USA).

2.2 Animal models

C57/Bl6 control mice and apoE−/− mice at 5 weeks of age were purchased from The Jackson Laboratory (Bar Harbor, ME, USA). All mice were housed under identical conditions in a sterile mouse facility; all procedures were performed according to protocols approved by the Institutional Animal Care and Use Committee (IACUC) of the University of Pennsylvania. Wild-type and apoE−/− mice were fed ad libitum for 12 weeks with standard mouse chow diet or high fat Western Diet, respectively (Harlan Teklad, Madison, WI, USA).

2.3 Synthesis of dextran-coated iron oxide nanoparticles (IONPs)

Dextran-coated IONPs were prepared through the co-precipitation of ferrous and ferric ions in the presence of dextran[12]. Dextran T-10 (12.5 g, 1.25 mmol) (Pharmacosmos A/S, Holbaek, Denmark) was dissolved in deionized water (dH_2O, 25 mL) and heated to 80 °C for 1 h. The solution was then allowed to cool to room temperature and stirred overnight. Subsequently, a solution of $FeCl_3$ (0.463 g, 3.65 mmol), and $FeCl_2$ (0.183 g, 1.13 mmol) in dH_2O (12.5 mL) was prepared and added to the dextran solution (50 mM). The combined solution was cooled on ice, degassed, and stirred under N_2 for 90 min. While stirring on ice under N_2, concentrated NH_4OH (15 mL) was added over 5 h using an automated syringe pump. The resulting viscous solution was heated to 90 °C for 1 h, cooled overnight, and centrifuged at 20,000×RCF for 30 min to remove large aggregates. Free iron and dextran were removed by diafiltration using a MidGee hoop cross flow cartridge (100 kDa molecular weight cutoff, GE Healthcare, USA). IONPs were diluted with dH_2O to afford a final concentration of 10 mg Fe/mL (180 mM). The Fe concentration of IONP solutions were determined by degrading and oxidizing an aliquot with HCl and hydrogen peroxide

NIH-PA Author Manuscript

NIH-PA Author Manuscript

NIH-PA Author Manuscript

(H_2O_2) and comparing optical absorbance measurements at 410 nm to a calibration curve, as described in [13].

The final IONP product (20 mL, 3.58 mmol, 10 mg Fe/mL) was combined with an equal volume of 10 M NaOH and mixed for 10 min. Epichlorohydrin (80 mL, 1.02 mol) (Sigma-Aldrich, St. Louis, MO, USA) was added and the solution vigorously stirred at room temperature overnight. Epichlorohydrin crosslinks the dextran coating within the IONPs, chemically activating the dextran surface for conjugation. The solution was then centrifuged (2,000×RCF, 10 min), and the clear upper phase containing unreacted epichlorohydrin was separated from the aqueous black IONP layer. The IONP layer was quickly purified via extraction in isopropanol. The IONP layer was combined with 5 volumes isopropanol and the mixture was vigorously shaken. Centrifugation of the mixture resulted in a layer of precipitated salt, a mid IONP layer, and an upper isopropanol layer (containing residual epichlorohydrin). The IONP layer was isolated and combined with an equal volume of concentrated NH_4OH and gently stirred for 24 h at room temperature, resulting in an aminated nanoparticle surface. Following synthesis, IONPs were filtered through a 0.2 μm nitrocellulose filter (Millipore, Bellerica, MA, USA) to remove any oversized material, and then further purified by diafiltration on a 100 kDa cutoff MidGee hoop.

2.4 Surface modification of IONPs with Bolton Hunter reagent

Aminated IONPs (1 mL in citrate buffer, pH 8, 2 mg Fe/mL) were reacted with three different concentrations of Sulfo-SHPP, (0.9 mM, 1.8 mM, and 3.6 mM) (Thermo Scientific Pierce, Rockford, IL, USA) in DMSO (100 μL), such that there was an excess of Sulfo-SHPP reagent to the number of nanoparticles (i.e., 50, 100 and 200-fold, respectively). The solution was stirred at room temperature overnight. The IONP solution was purified from excess reactants using a 50K MWCO Amicon-Ultracentrifuge filter device (Millipore Inc., Bellerica, MA, USA). To ensure that every amine group was blocked, SHPP-modified dextran-coated IONPs (1 mL, 2 mg Fe/mL; $IONP_{50}$, $IONP_{100}$ and $IONP_{200}$) were reacted with succinic anhydrate (4.4 mg, 4.4 mmol) in DMF (200 μL). IONPs were purified by ultracentrifugation methods, as mentioned above.

2.5 Physicochemical characterization of IONPs

An IONP stock sample (2 mg Fe/mL) was diluted in dH_2O and deposited on 200-mesh carbon coated copper grids (Polysciences, Warrington, PA, USA) for TEM imaging with a JEOL 1010 transmission electron microscope operating at 80 kV. Mean iron core size was determined by measuring the diameter of 100 individual nanoparticles. Imaging analysis was performed with Image J software (NIH). The stock sample of IONPs was diluted in phosphate buffered saline (pH 7.4 – Invitrogen, Carlsbad, CA, USA) for determination of hydrodynamic diameter by DLS – as recorded on a Zetasizer Nano-ZS (Malvern Instruments, UK) using the non-invasive back-scatter (NIBS) mode. Zeta potential measurements were also measured using a Zetasizer Nano-ZS.

2.6 Radioiodination of SHPP-IONPs

A solution of SHPP-IONPs (0.2 mg Fe in 100 μL of PBS) was combined with a chloramine-T oxidant solution in PBS (2 μL, 17.6 mM) and [^{125}I]NaI (1 mCi (37 MBq) diluted to 10 μL

NIH-PA Author Manuscript

NIH-PA Author Manuscript

NIH-PA Author Manuscript

in PBS) for 30 minutes with stirring. Unreacted free radioiodide ^{125}I was removed by ultracentrifugation as described above. The labeling yield was monitored by DAR (FLA-7000, FujiFilm Phosphorimager, Tokyo, Japan) of radioTLC SiO_2 silica gel plates. TLC plates were run in 1:1 10% ammonium acetate/methanol and exposed for approximately 15 min to the phosphor plate (BAS 2000, FijiFilm) before imaging.

2.7 Radiolabel stability of [^{125}I]IONPs

An aliquot of [^{125}I]IONPs (20 μL, 2 μCi, 2 mg Fe/mL) was added to eppendorf tubes containing either 100 μL PBS or 0.2% wt/vol Pronase (Sigma-Aldrich, St. Louis, MO, USA). Triplicate samples were then placed on a rotoshaker at 37 °C. Following incubation for 0 min, 5 min, 15 min, 30 min, 60 min, 2h, 4h, 6h, 24 h, 48 h, and 72 h, a 1 μL sample was spotted for radio-TLC and DAR as discussed above.

2.8 In vivo blood pharmacokinetics of [^{125}I]IONPs

[^{125}I]IONPs (100 μL, 10 μCi, 0.2 mg Fe/mL) were administrated intravenously to naive C57/Bl6 mice (n = 3) via tail vein injection. Blood samples (approximately 10 μL each) were collected via retro-orbital bleeding at 5 min, 15 min, 30 min, 60 min, 2 h, 4 h, 8 h, 24 h, 48 h, and 72 h post [^{125}I]IONP administration. Each sample was weighed and radioactivity was measured with a gamma γ) counter and normalized to the injected dose (2470 Wizard, Perkin Elmer, Wallac Oy, Turku, Finland). Data are reported as percent of injected dose per gram of blood (%ID/g).

2.9 In vivo biodistribution

Two animal cohorts, each containing 16 mice (n =4 per time point) were used for biodistribution studies. Briefly, [^{125}I]IONPs (100 μL, 10 μCi, 0.2 mg Fe/mL) were injected intravenously to the control C57/Bl6 or apoE−/− mice. After 6, 24, 48, and 72 h, mice were euthanized and organs were harvested. Tissues were dried, weighed, and their radioactivity concentration was measured using a γ-counter. Organ activity levels were further normalized to the amount of radioactivity in the injected dose, with results expressed as percent of injected dose/g of tissue (%ID/g).

2.10 Digital autoradiography (DAR) of heart sections

For DAR experiments, control mice and apoE−/− mice (n = 3 per group) were injected intravenously with [^{125}I]IONPs (100 μL, 20 μCi, 0.2 mg Fe/mL), and their hearts were isolated 72 h post-injection. Briefly, mice were anesthetized with isoflurane, sacrificed, and then hearts were perfused in situ with heparinized saline (15 mL, 10 units/mL) followed by 1:1 PBS/optimum cutting temperature compound (OCT, TissueTek, 15 mL). Isolated hearts were frozen on dry-ice and stored at −80 °C before slices were prepared. Serial 80 μm-thick transverse heart sections were prepared using a cryomicrotome Leica CM1950 (Leica Microsystems, Inc, Buffalo Grove, IL, USA). Slices were mounted on glass slides, and exposed for ~66 h to phosphor plates prior to imaging by DAR.

NIH-PA Author Manuscript

NIH-PA Author Manuscript

NIH-PA Author Manuscript

2.11 Statistical analysis

All data are expressed as mean ± standard deviation (S.D.). Means between the various groups were compared for differences with analysis of variance. In situations of multiple comparisons, a *post hoc* Bonferroni correction was applied. *P*-values < 0.05 were interpreted, representing a statistically significant difference. All data were analyzed by GraphPad PRISM version 5.0 software.

3 Results

3.1 Synthesis and characterization of IONPs

[^{125}I]IONPs were synthesized as disclosed in Figure 1. The synthesis of dextran-coated IONPs followed previously published procedures [12] affording IONPs with a 27.5 nm average hydrodynamic diameter (D_{avg}) by DLS, and zeta potential of −14.5 mV. By TEM, the iron oxide core diameter was measured to be 12.0 nm ± 2.3 nm. After IONP synthesis, particles were aminated resulting in positively charged nanoparticles with a zeta potential of approximately +6 mV. The average hydrodynamic diameter following amination, determined by DLS, was 28 nm. TEM analysis revealed a core size of 12.2 nm ± 1.9 nm.

SHPP-IONPs were successfully obtained following the scheme shown in Figure 1. As previously described, three different concentration of Sulfo-SHPP were used to prepare SPPH-IONPs (50-, 100-, and 200-molar excess of Sulfo-SHPP). All nanoparticle formulations ($IONP_{50}$, $IONP_{100}$ and $IONP_{200}$) had no significant change in D_{avg} after coupling, while zeta potential was drastically altered to negative values (~ −7mV), indicating that SHPP-modified IONP was prepared (Table 1). Then, all IONP formulations were reacted with succinic anhydride following conjugation with Sulfo-SHPP reagent to further impart a negative surface charge (approximately −21 mV for all formulations).

The D_{avg} of $IONP_{50}$, $IONP_{100}$, and $IONP_{200}$ was analyzed by DLS. All three IONP formulations had D_{avg} ~30 nm as shown in Figure 2A. Specifically, $IONP_{50}$ had an average diameter of 31.8 nm, $IONP_{100}$ 32.2 nm, and $IONP_{200}$ 33.7 nm. All three formulations exhibited low polydispersity indexes, 0.154, 0.157, and 0.137 for $IONP_{50}$, $IONP_{100}$ and $IONP_{200}$ respectively (Table 1). The mean core size for all IONPs was further determined by TEM. A representative micrograph and distribution of cores is shown in Figure 2B. The mean core diameter for all of the IONP formulations was approximately 13 nm, confirming that SHPP surface modification did not alter nanoparticle size.

3.2 Radiolabeling and radiochemical stability

Radiolabeling with ^{125}I occurred readily on the SHPP-modified IONPs by electrophilic aromatic substitution [14–15]. Radiolabeling yields of ~25% were achievable for [^{125}I]$IONP_{50}$, and $IONP_{100}$. $IONP_{200}$ had improved labeling efficiency (~50%), likely due to an increased number of available SHPP sites for the iodine to bind. After radiolabeling, all three nanoparticle formulations were purified by ultracentrifugation, resulting in high radiochemical purity (>96%). Due to higher $IONP_{200}$ labeling yields, these NPs were selected for further *in vitro* and *in vivo* experiments.

NIH-PA Author Manuscript

NIH-PA Author Manuscript

NIH-PA Author Manuscript

Radiochemical stability of $IONPs_{200}$ was evaluated for up to 48 h in PBS (control) or 0.2 wt %/vol Pronase at 37 °C. Figure 3 demonstrates minimal radiolabel degradation over 48 h, indicating the nanoparticle's suitability for *in vivo* studies.

3.3 Circulation time

Blood levels of the $[^{125}I]IONP_{200}$ declined in a biphasic manner, with an α half-life of 38.0 min and β half-life of 871.5 min (Figure 4). Therefore, $[^{125}I]$IONPs exhibited blood circulation times that were expected to be long enough for accumulation and detection. Acquisition of a clearance profile was necessary to identify times at which little to no nanoparticles remain in circulation to select times where background levels would not interfere with optimal visualization of macrophage at the target sites.

3.4 Biodistribution studies and DAR

The biodistribution data for $[^{125}I]IONP_{200}$ were generated in both healthy and atherosclerotic mice (Tables 2 and 3). $IONP_{200}$ showed significant uptake in both the liver and spleen due to the high content of phagocytic cells in these organs. Thyroid uptake was also evaluated to determine *in vivo* radiolabel deiodination. Thyroid exhibited very low levels of radioactivity, even after long periods, indicating *in vivo* radiolabel stability. These findings showed that iodine-labeled nanoparticles remained stable over the course of imaging; therefore, providing evidence for the fate and location of the nanoparticles in various anatomic sites.

The uptake of $[^{125}I]IONP_{200}$ in the hearts of apoE−/− mice was higher than that obtained for healthy mice (Fig. 5A). At 72 h post-injection, the heart uptake in atherosclerotic animals was higher than most other organs, including blood. Noteworthy was the heart-to-blood ratio at 72 h post-injection from atherosclerotic mice, which was significantly higher than the value obtained from healthy mice at the same time point. Moreover, when heart-to-blood ratios were calculated for apoE −/− mice during the entire experiment, 72 h post-injection showed the highest signal-to-noise ratio (Figure 5B). These findings suggest IONPs are taken up by the macrophage-rich tissues, such as atherosclerotic plaques where high concentration of such cells resides.

To further confirm the specific accumulation of $[^{125}I]IONP_{200}$ within the hearts of apoE−/− mice, DAR was performed on slices obtained from healthy hearts and diseased hearts. We were able to demonstrate high levels of radiotracer signal from the hearts of apoE −/− mice, while no signal was observed in the healthy mice (Fig. 5C). This finding may suggest that $[^{125}I]IONP_{200}$ particles remain in the targeted sites (atherosclerotic plaques), while they are substantially cleared in the healthy heart and normal tissues.

4 Discussion

Up until now, assessment of presence of atherosclerotic plaques in the coronary arteries has been primarily based upon visualization by structural imaging such as coronary arteriography (by conventional angiographic techniques), by CT angiography [16–17], or by cardiac perfusion imaging [18–19]. While these techniques are of value in detecting moderate to severe atherosclerotic disorders that result in significant narrowing of the

NIH-PA Author Manuscript

NIH-PA Author Manuscript

NIH-PA Author Manuscript

arteries, they fail to detect the beginning of the disease process which is amenable to early treatment with the established drugs. It is clear that, when the disease is detected in advanced stages by radiographic or nuclear medicine techniques, restoration of blood flow to the myocardium will require invasive angiographic techniques or surgical procedures in most circumstances. In the past decade, efforts have been made to detect atherosclerosis at the cellular level by molecular imaging techniques that are based on PET [18, 20]. Early reports during the past decade described the uptake of FDG, a glucose analogue, by macrophages in the plaques in various locations in the major arteries including the carotids, aorta and lower extremities [21–22]. The successful application of this technique has resulted in early and accurate detection of this disorder in these structures[23]. Efforts have been made to combine the degree of structural abnormalities such as the thickness of aortic wall as measured by CT with cellular assessment of plaque activity as determined by PET as an indicator of atherosclerotic burden (atheroburden) [24]. This methodology has been effectively used to measure response to treatment, particularly in the carotid arteries [25]. However, because of the intense uptake of FDG in myocardial muscles, cardiac motion, and the small size of coronary arteries, the use of this approach is quite limited in the heart. Therefore, alternate approaches need to be explored to detect atherosclerotic plaques in the heart in its early stages, which would allow for early intervention and prevention from further progression to irreversible disease and serious complications such as myocardial infarction.

The ability to image macrophage burden within atherosclerotic plaques using radiolabeled nanoparticles requires nanoparticle formulations that are small, capable of extravasating the capillaries, and remain in the circulation for an extended period of time for incorporation into macrophages at various sites [26]. It is well established that NP below 100 nm in size are phagocytized by macrophages preferentially and are not heavily taken up in the reticuloendothelial system cells (RES) in the liver and the spleen, and therefore, can be effectively used to detect atherosclerotic plaques in either the major vessels or in the heart[27]. Generally, nanoparticles larger than 200 nm in diameter are rapidly cleared via the RES system, while nanoparticles smaller than 10 nm undergo renal filtration[28]. Therefore, nanoparticles with diameters between 10–100 nm are preferred due to longer circulation times, and thus, higher accumulation at the target site [29–30]. Efficient accumulation within plaques favors long-circulating nanoparticles since enhanced vascular permeability in inflamed areas promotes nanoparticle penetration into atherosclerotic lesions, leading to access of the IONPs to macrophages [2]. In addition, negatively charged particles preferentially associate with phagocytic cells due to higher opsonin adsorption. Therefore, they are often avidly phagocytosed by macrophages in atherosclerotic plaques[31]. Reports in the literature have primarily dealt with MRI and iron oxide particles in this setting[32]. Unfortunately, because of the low sensitivity of MR imaging in detecting signals from the contrast agents, a large amount of such preparations (including iron oxide particles) should be administered intravenously to generate reliable and interpretable results[32]. This has resulted in serious side effects that have raised questions about their routine use as safe preparations.

Radiolabeled NP imaging techniques will provide an alternative approach for this purpose because of their high sensitivity for detecting the disease process without any noticeable

NIH-PA Author Manuscript

NIH-PA Author Manuscript

NIH-PA Author Manuscript

delirious effects from preparations employed for this purpose. This has proven to be the case with many other tracers that have been used in the past [28]. PET-based tracers appear to be very attractive for overcoming the deficiencies that are associated with MR/CT-based contrast enhancement agents [33–34]. In addition, PET provides optimal quantification that cannot be achieved by radiologic techniques [35–36]. In recent years, some efforts have been successful in visualizing plaque with positron emitting NP, especially in the major vessels. No attempts have been made to utilize radiolabeled NP to visualize plaques in the coronary arteries because of difficulties related to the low spatial resolution of PET and the constant motion of this organ.

To overcome these deficiencies, we have decided to adopt a new approach that we have tested successfully in other organs that are commonly affected by diffuse disease processes [36–37]. In particular, we have used this approach in assessing global calcification in the coronary arteries in the heart with great success [38–39] and now we have decided to apply this methodology for detecting plaques in this organ. In this report, we have described our approach by measuring the uptake of NP in the entire heart in an experimental mice model. We have clearly shown that this approach will allow separating animals with diffuse atherosclerosis from the control group. Therefore, we believe that *in vivo* imaging with this technique will allow us to detect atherosclerotic plaques in the heart during the very early stages of disease and hope that this will lead to early intervention and optimal outcome in the affected population. We plan to proceed with these experiments on a larger scale in both animals and human beings in the future. We are relatively optimistic about the potential role of this technology in diagnosing this serious and deadly disease and preventing serious complications and mortality that are associated with this medical problem.

We recognize that there are certain limitations to this research study. First, there is a report indicating leukocyte recruitment to the arterial wall of 57BL/6 mice, which was not related to atherosclerosis process [40]. Since we did not employ an apoE−/− mice model that were on a normal diet, we cannot exclude the possibility of non-atherosclerosis artery inflammation based on this design and further studies will be required to determine the differential effects of the high-fat western and normal diets on the apoE−/− mice. However, regardless if the type and source of macrophage recruitment to the arterial wall with this preparation, we were able to demonstrate the presence of inflammation in the heart. In addition, based on available data, there is no biologically plausible reason other than coronary artery macrophage uptake that can explain the accumulation of IONPs in the heart of these apoE−/− mice. Yet, further studies are necessary to elucidate the origin of arterial wall uptake in this murine model. Second, since the heart autoradiographic slices that were generated in this study were too thick for histological examination, we were not able to confirm atherosclerotic plaque formations by this technique. However, it should be noted that the high fat western diet is known to result in atheroma formation in the apoE−/− mice model, which has been employed in many investigations. Also, since our main objective was to demonstrate the feasibility of detecting atherosclerosis in the coronary arteries, we did not examine other arteries including aorta which is common site of disease in this model.

NIH-PA Author Manuscript
NIH-PA Author Manuscript
NIH-PA Author Manuscript

5 Conclusions

This scientific communication describes the preliminary results of utilizing an iron oxide nanoparticle labeled with ^{125}I via Bolton-Hunter conjugation ([^{125}I]IONPs) in mice. This preparation possesses adequate physical-chemical properties for *in vivo* studies, such as small size (~30 nm), good radiolabel stability, and long circulation times, leading to significant accumulation in the atherosclerotic plaques of apoE−/− mice compared with healthy controls. These findings suggest radiolabeled dextran-coated iron oxide nanoparticles may have potential to become a tool to detect macrophages in the atherosclerosis plaques of coronary arteries; however, these preliminary findings should be confirmed by further studies.

Acknowledgments

The authors would like to thank Conselho Nacional de Desenvolvimento Científico e Tecnológico (CNPq) – Brazil and Comissão Nacional de Energia Nuclear (CNEN) – Brazil for providing a scholarship to André Luís Branco de Barros. Special thanks to Catherine Hou for assistance with cryomicrotome. This work was supported in part by the National Institute of Health NIBIB/R01-EB012065 (AT) and NCI/R01-CA157766 (AT).

References

1. Gupta AS. Nanomedicine approaches in vascular disease: a review. Nanomedicine: nanotechnology, biology, and medicine. 2011; 7:763–779.
2. Morishige K, Kacher DF, Libby P, et al. High-resolution magnetic resonance imaging enhanced with superparamagnetic nanoparticles measures macrophage burden in atherosclerosis. Circulation. 2010; 122:1707–1715. [PubMed: 20937980]
3. Libby P. Inflammation in atherosclerosis. Nature. 2002; 420:868–874. [PubMed: 12490960]
4. Amirbekian V, Lipinski MJ, Briley-Saebo KC, et al. Detecting and assessing macrophages in vivo to evaluate atherosclerosis noninvasively using molecular MRI. Proceedings of the National Academy of Sciences of the United States of America. 2007; 104:961–966. [PubMed: 17215360]
5. Kuroiwa Y, Yamashita A, Miyati T, et al. Atherosclerotic lesions rich in macrophages or smooth muscle cells discriminated in rabbit iliac arteries based on T1 relaxation time and lipid content. Academic radiology. 2010; 17:230–238. [PubMed: 19910212]
6. Moore KJ, Tabas I. Macrophages in the pathogenesis of atherosclerosis. Cell. 2011; 145:341–355. [PubMed: 21529710]
7. Verschuren L, Kleemann R, Offerman EH, et al. Effect of low dose atorvastatin versus diet-induced cholesterol lowering on atherosclerotic lesion progression and inflammation in apolipoprotein E*3-Leiden transgenic mice. Arteriosclerosis, thrombosis, and vascular biology. 2005; 25:161–167.
8. Jaffer FA, Libby P, Weissleder R. Optical and multimodality molecular imaging: insights into atherosclerosis. Arteriosclerosis, thrombosis, and vascular biology. 2009; 29:1017–1024.
9. Ruehm SG, Corot C, Vogt P, Kolb S, Debatin JF. Magnetic resonance imaging of atherosclerotic plaque with ultrasmall superparamagnetic particles of iron oxide in hyperlipidemic rabbits. Circulation. 2001; 103:415–422. [PubMed: 11157694]
10. Nahrendorf M, Keliher E, Marinelli B, et al. Detection of macrophages in aortic aneurysms by nanoparticle positron emission tomography-computed tomography. Arteriosclerosis, thrombosis, and vascular biology. 2011; 31:750–757.
11. Nahrendorf M, Zhang H, Hembrador S, et al. Nanoparticle PET-CT imaging of macrophages in inflammatory atherosclerosis. Circulation. 2008; 117:379–387. [PubMed: 18158358]
12. Thorek DL, Tsourkas A. Size, charge and concentration dependent uptake of iron oxide particles by non-phagocytic cells. Biomaterials. 2008; 29:3583–3590. [PubMed: 18533252]
13. Moore A, Josephson L, Bhorade RM, Basilion JP, Weissleder R. Human transferrin receptor gene as a marker gene for MR imaging. Radiology. 2001; 221:244–250. [PubMed: 11568347]

NIH-PA Author Manuscript

NIH-PA Author Manuscript

NIH-PA Author Manuscript

14. Bolton AE, Hunter WM. The labelling of proteins to high specific radioactivities by conjugation to a 125I-containing acylating agent. The Biochemical journal. 1973; 133:529–539. [PubMed: 4733239]
15. Simone EA, Zern BJ, Chacko AM, et al. Endothelial targeting of polymeric nanoparticles stably labeled with the PET imaging radioisotope iodine-124. Biomaterials. 2012; 33:5406–5413. [PubMed: 22560201]
16. Salavati A, Radmanesh F, Heidari K, Dwamena BA, Kelly AM, Cronin P. Dual-source computed tomography angiography for diagnosis and assessment of coronary artery disease: systematic review and meta-analysis. Journal of cardiovascular computed tomography. 2012; 6:78–90. [PubMed: 22226727]
17. Salavati A, Rybicki FJ. Evidence for prospective ECG-triggering coronary CT angiography in routine practice. The international journal of cardiovascular imaging. 2012; 28:2121–2124. [PubMed: 22318542]
18. Pakkal M, Raj V, McCann GP. Non-invasive imaging in coronary artery disease including anatomical and functional evaluation of ischaemia and viability assessment. The British journal of radiology. 2011; 84(Spec No 3):S280–295. [PubMed: 22723535]
19. Salavati A, Radmanesh F, Esfahani SA. Diagnostic accuracy and clinical utility of noninvasive testing for coronary artery disease. Annals of internal medicine. 2011; 154:290. author reply 290. [PubMed: 21320946]
20. Botvinick EH, Perini R, Bural G, et al. The aging of the heart and blood vessels: a consideration of anatomy and physiology in the era of computed tomography, magnetic resonance imaging, and positron emission tomographic imaging methods with special consideration of atherogenesis. Seminars in nuclear medicine. 2007; 37:120–143. [PubMed: 17289459]
21. Yun M, Jang S, Cucchiara A, Newberg AB, Alavi A. 18F FDG uptake in the large arteries: a correlation study with the atherogenic risk factors. Seminars in nuclear medicine. 2002; 32:70–76. [PubMed: 11839072]
22. Yun M, Yeh D, Araujo LI, Jang S, Newberg A, Alavi A. F-18 FDG uptake in the large arteries: a new observation. Clinical nuclear medicine. 2001; 26:314–319. [PubMed: 11290891]
23. Mehta NN, Torigian DA, Gelfand JM, Saboury B, Alavi A. Quantification of atherosclerotic plaque activity and vascular inflammation using [18-F] fluorodeoxyglucose positron emission tomography/computed tomography (FDG-PET/CT). Journal of visualized experiments: JoVE. 2012:e3777. [PubMed: 22588186]
24. Bural GG, Torigian DA, Chamroonrat W, et al. Quantitative assessment of the atherosclerotic burden of the aorta by combined FDG-PET and CT image analysis: a new concept. Nuclear medicine and biology. 2006; 33:1037–1043. [PubMed: 17127178]
25. Tahara N, Kai H, Ishibashi M, et al. Simvastatin attenuates plaque inflammation: evaluation by fluorodeoxyglucose positron emission tomography. Journal of the American College of Cardiology. 2006; 48:1825–1831. [PubMed: 17084257]
26. Jokerst JV, Lobovkina T, Zare RN, Gambhir SS. Nanoparticle PEGylation for imaging and therapy. Nanomedicine (Lond). 2011; 6:715–728. [PubMed: 21718180]
27. Duan X, Li Y. Physicochemical characteristics of nanoparticles affect circulation, biodistribution, cellular internalization, and trafficking. Small. 2013; 9:1521–1532. [PubMed: 23019091]
28. de Barros AB, Tsourkas A, Saboury B, Cardoso VN, Alavi A. Emerging role of radiolabeled nanoparticles as an effective diagnostic technique. EJNMMI research. 2012; 2:39. [PubMed: 22809406]
29. Neuberger T, Schöpf B, Hofmann H, Hofmann M, von Rechenberg B. Superparamagnetic nanoparticles for biomedical applications: Possibilities and limitations of a new drug delivery system. Journal of Magnetism and Magnetic Materials. 2005; 293:483–496.
30. Laurent S, Forge D, Port M, et al. Magnetic iron oxide nanoparticles: synthesis, stabilization, vectorization, physicochemical characterizations, and biological applications. Chemical reviews. 2008; 108:2064–2110. [PubMed: 18543879]
31. Moghimi SM, Hunter AC, Murray JC. Long-circulating and target-specific nanoparticles: theory to practice. Pharmacological reviews. 2001; 53:283–318. [PubMed: 11356986]

NIH-PA Author Manuscript

NIH-PA Author Manuscript

NIH-PA Author Manuscript

32. Kanwar RK, Chaudhary R, Tsuzuki T, Kanwar JR. Emerging engineered magnetic nanoparticulate probes for molecular MRI of atherosclerosis: how far have we come? Nanomedicine (Lond). 2012; 7:899–916. [PubMed: 22715913]
33. Alavi A, Lakhani P, Mavi A, Kung JW, Zhuang H. PET: a revolution in medical imaging. Radiologic clinics of North America. 2004; 42:983–1001. vii. [PubMed: 15488553]
34. Zaidi H, Montandon ML, Alavi A. The clinical role of fusion imaging using PET, CT, and MR imaging. Magnetic resonance imaging clinics of North America. 2010; 18:133–149. [PubMed: 19962098]
35. Acton PD, Zhuang H, Alavi A. Quantification in PET. Radiologic clinics of North America. 2004; 42:1055–1062. viii. [PubMed: 15488557]
36. Basu S, Zaidi H, Houseni M, et al. Novel quantitative techniques for assessing regional and global function and structure based on modern imaging modalities: implications for normal variation, aging and diseased states. Seminars in nuclear medicine. 2007; 37:223–239. [PubMed: 17418154]
37. Alavi A, Newberg AB, Souder E, Berlin JA. Quantitative analysis of PET and MRI data in normal aging and Alzheimer's disease: atrophy weighted total brain metabolism and absolute whole brain metabolism as reliable discriminators. Journal of nuclear medicine: official publication, Society of Nuclear Medicine. 1993; 34:1681–1687.
38. Beheshti M, Saboury B, Mehta NN, et al. Detection and global quantification of cardiovascular molecular calcification by fluoro18-fluoride positron emission tomography/computed tomography--a novel concept. Hellenic journal of nuclear medicine. 2011; 14:114–120. [PubMed: 21761011]
39. Basu S, Hoilund-Carlsen PF, Alavi A. Assessing global cardiovascular molecular calcification with 18F-fluoride PET/CT: will this become a clinical reality and a challenge to CT calcification scoring? European journal of nuclear medicine and molecular imaging. 2012; 39:660–664. [PubMed: 22274730]
40. Hagita S, Osaka M, Shimokado K, Yoshida M. Adipose inflammation initiates recruitment of leukocytes to mouse femoral artery: role of adipo-vascular axis in chronic inflammation. PloS one. 2011; 6:e19871. [PubMed: 21625491]

NIH-PA Author Manuscript
NIH-PA Author Manuscript
NIH-PA Author Manuscript

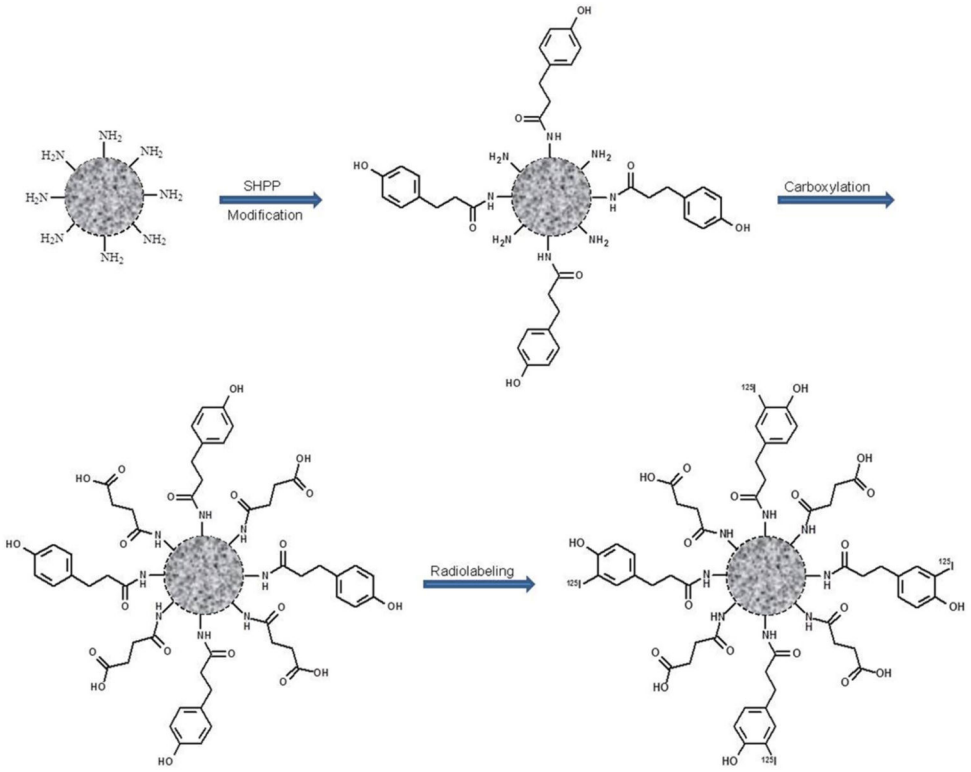

FIGURE 1.
Synthesis of [^{125}I]IONPs.

NIH-PA Author Manuscript

NIH-PA Author Manuscript

NIH-PA Author Manuscript

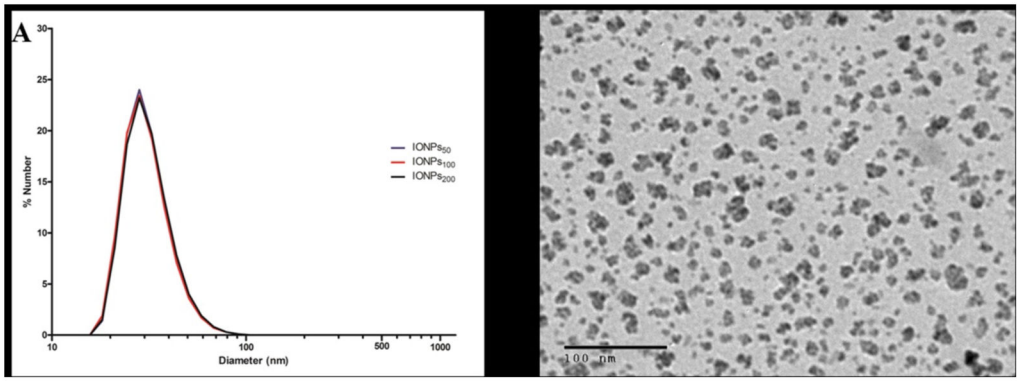

FIGURE 2.

Dynamic Light Scattering (DLS) size distribution and TEM image. (A) DLS size distribution for $IONP_{50}$, $IONP_{100}$, and $IONP_{200}$. Three IONP formulations investigated show identical size distribution. (B) Representative TEM image of $IONP_{200}$ (core size: 13.9 nm ± 2.7 nm). Scale bar: 100 nm.

NIH-PA Author Manuscript
NIH-PA Author Manuscript
NIH-PA Author Manuscript

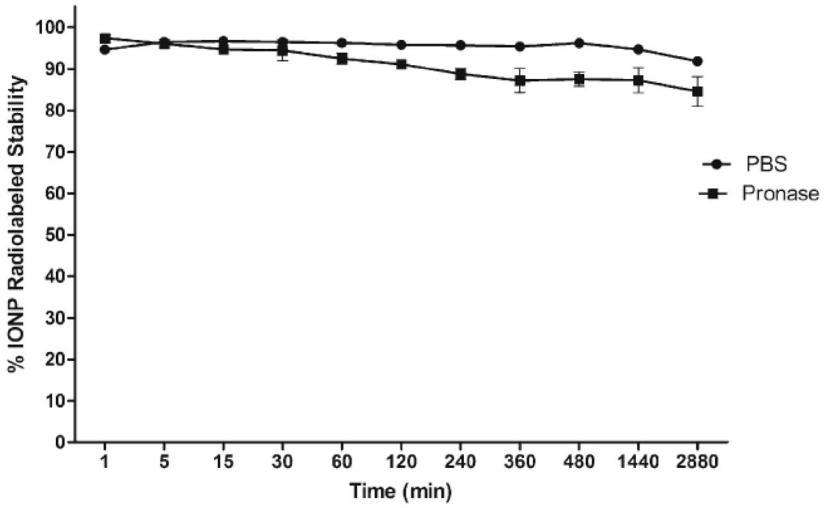

FIGURE 3.
Radiolabel stability of [^{125}I]IONPs in PBS and 0.2 wt%/vol Pronase at 37 °C.

NIH-PA Author Manuscript

NIH-PA Author Manuscript

NIH-PA Author Manuscript

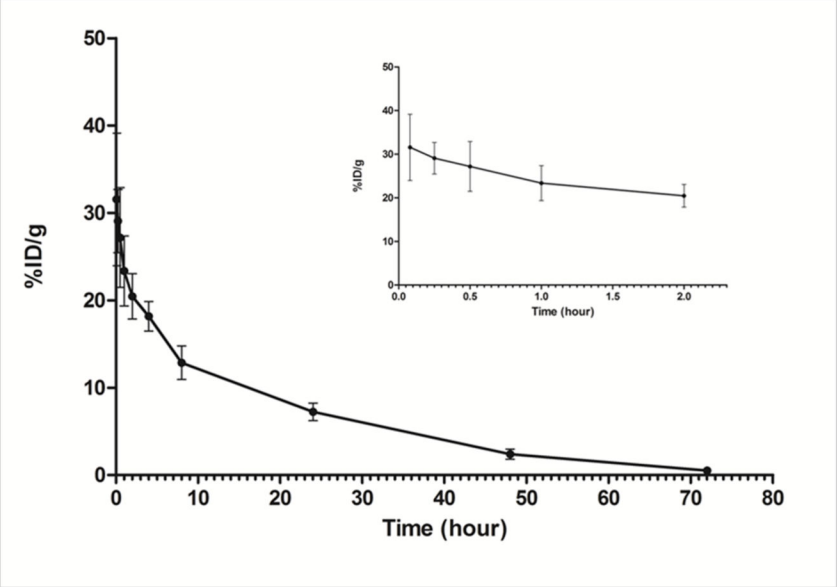

FIGURE 4.

Blood clearance profile of [^{125}I]IONP$_{200}$ (10 μCi) following intravenous tail-vein andministration to each healthy mouse (n = 3). Blood samples were collected by retro-orbital bleeding at specific time points. (Inset: Blood clearance over the first two hours).

NIH-PA Author Manuscript
NIH-PA Author Manuscript
NIH-PA Author Manuscript

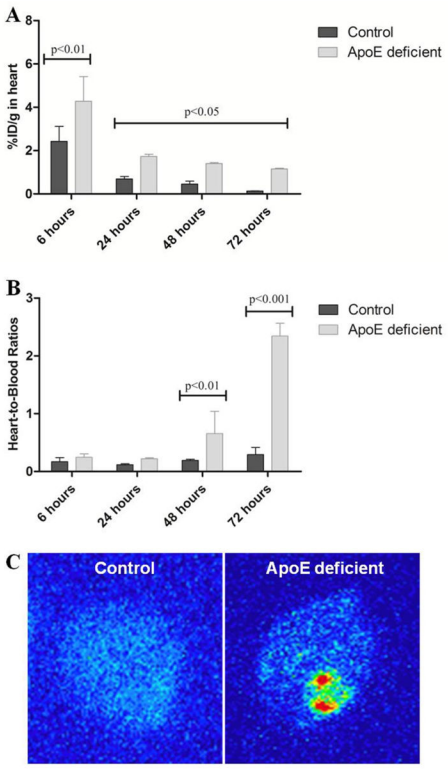

FIGURE 5.

Heart uptake and DAR from control and apoE −/− mice. (A) Mean heart uptake obtained after intravenous administration of [^{125}I]IONPs into healthy and atherosclerotic mice (*n*=4). (B) Mean heart-to-blood ratios obtained after intravenous administration of [^{125}I]IONPs into healthy and atherosclerotic mice (*n*=4). (C) DAR obtained from heart of healthy and atherosclerotic mice, respectively, at 72 h post-injection of [^{125}I]IONPs (20 μCi, 0.8 mg Fe/kg).

NIH-PA Author Manuscript
NIH-PA Author Manuscript
NIH-PA Author Manuscript

Mol Imaging Biol. Author manuscript; available in PMC 2015 June 01.

TABLE 1

Characterization of the three IONPs after each stage of synthesis.

Formulation		Mean diameter (nm)*	Polydispersity index (PDI)	Zeta Potential (mV)	Core size (nm)†
$IONP_{50}$	Aminated	28.1	0.159	+5.9	12.2 ± 1.9
	SHPP	33.1	0.221	−5.4	14.0 ± 2.2
	Carboxylated SHPP	31.8	0.154	−20.6	13.4 ± 1.7
$IONP_{100}$	Aminated	28.1	0.159	+5.9	12.2 ± 1.9
	SHPP	34.7	0.198	−6.8	11.9 ± 3.0
	Carboxylated SHPP	32.2	0.157	−21.2	13.7 ± 1.2
$IONP_{200}$	Aminated	28.1	0.159	+5.9	12.2 ± 1.9
	SHPP	31.8	0.211	−8.2	12.9 ± 1.5
	Carboxylated SHPP	33.6	0.137	−22.0	13.9 ± 2.7

*Determined by means of DLS.

†Determined by means of TEM.

NIH-PA Author Manuscript

NIH-PA Author Manuscript

NIH-PA Author Manuscript

TABLE 2

Biodistribution of [^{125}I]IONPs in healthy mice*.

Tissue	6 hours	24 hours	48 hours	72 hours
Blood	14.97 ± 2.86	5.91 ± 0.52	2.39 ± 0.58	0.51 ± 0.15
Heart	2.43 ± 0.69	0.69 ± 0.11	0.46 ± 0.13	0.14 ± 0.01
Lung	3.09 ± 0.72	1.57 ± 0.50	1.51 ± 0.26	0.49 ± 0.13
Kidneys	1.45 ± 0.30	0.93 ± 0.14	1.43 ± 0.14	0.72 ± 0.25
Spleen	11.15 ± 0.93	12.14 ± 1.63	21.32 ± 3.05	11.46 ± 4.67
Liver	21.87 ± 2.91	19.90 ± 4.88	31.33 ± 2.76	24.79 ± 6.36
Skin	1.48 ± 0.28	0.78 ± 0.12	0.61 ± 0.16	0.60 ± 0.12
Muscle	0.30 ± 0.02	0.24 ± 0.01	0.30 ± 0.13	0.16 ± 0.05
Bone	0.36 ± 0.06	0.33 ± 0.06	0.63 ± 0.11	0.38 ± 0.08
Thyroid†	0.53 ± 0.01	0.60 ± 0.11	0.46 ± 0.15	0.59 ± 0.09
Brain	0.35 ± 0.06	0.14 ± 0.03	0.09 ± 0.02	0.03 ± 0.01
Stomach	1.75 ± 0.91	0.47 ± 0.11	0.46 ± 0.20	0.34 ± 0.17
Small Intestine	1.18 ± 0.07	0.88 ± 0.37	1.47 ± 0.27	0.88 ± 0.39
Large Intestine	1.05 ± 0.26	0.70 ± 0.36	0.47 ± 0.24	0.39 ± 0.10

*All data are reported as mean ± S.D. % ID/g tissue of [^{125}I]IONPs (n = 4)

†Thyroid uptake is reported as mean ± S.D. % ID/organ of [^{125}I]IONPs (n = 4)

NIH-PA Author Manuscript

NIH-PA Author Manuscript

NIH-PA Author Manuscript

TABLE 3

Biodistribution of [^{125}I]IONPs in apoE−/−*

Tissue	6 hours	24 hours	48 hours	72 hours
Blood	17.41 ± 1.24	8.01 ± 1.12	2.66 ± 1.22	0.50 ± 0.05
Heart	4.27 ± 1.15	1.73 ± 0.10	1.41 ± 0.05	1.15 ± 0.03
Lung	4.92 ± 0.72	2.13 ± 0.77	1.30 ± 0.54	0.75 ± 0.23
Kidneys	2.21 ± 0.30	1.56 ± 0.42	1.04 ± 0.24	0.85 ± 0.15
Spleen	8.37 ± 2.02	17.39 ± 4.18	14.21 ± 2.75	17.13 ± 5.63
Liver	22.68 ± 5.53	36.25 ± 4.49	36.93 ± 4.74	35.75 ± 1.25
Skin	1.42 ± 0.36	0.45 ± 0.23	0.45 ± 0.20	0.25 ± 0.10
Muscle	0.56 ± 0.20	0.48 ± 0.23	0.25 ± 0.07	0.21 ± 0.05
Bone	0.56 ± 0.09	0.59 ± 0.15	0.39 ± 0.09	0.37 ± 0.13
Thyroid†	0.21 ± 0.08	0.57 ± 0.15	0.59 ± 0.08	0.47 ± 0.09
Brain	0.39 ± 0.04	0.17 ± 0.05	0.11 ± 0.06	0.05 ± 0.01
Stomach	1.86 ± 0.22	0.71 ± 0.34	0.61 ± 0.09	0.47 ± 0.21
Small Intestine	1.29 ± 0.37	0.82 ± 0.28	0.59 ± 0.17	0.45 ± 0.10
Large Intestine	1.08 ± 0.29	0.92 ± 0.25	0.38 ± 0.09	0.43 ± 0.11

*All data are reported as mean ± S.D. % ID/g tissue of [^{125}I]IONPs (n = 4)

†Thyroid uptake is reported as mean ± S.D. % ID/organ of [^{125}I]IONPs (n = 4)